PAPER

Check for updates

Electrospun single-phase spinel magnetic high entropy oxide nanoparticles *via* low-temperature ambient annealing†

Xiao Han,[a] Dian Li,[b] Jingyi Zhou,[c] Yufeng Zheng,[b] Lingyan Kong,[c] Lin Li[d] and Feng Yan [ID] *[d]

High entropy oxide nanoparticles (HEO NPs) with multiple component elements possess improved stability and multiple uses for functional applications, including catalysis, data memory, and energy storage. However, the synthesis of homogenous HEO NPs containing five or more immiscible elements with a single-phase structure is still a great challenge due to the strict synthetic conditions. In particular, several synthesis methods of HEO NPs require extremely high temperatures. In this study, we demonstrate a low cost, facile, and effective method to synthesize three- to eight-element HEO nanoparticles by a combination of electrospinning and low-temperature ambient annealing. HEO NPs were generated by annealing nanofibers at 330 °C for 30 minutes under air conditions. The average size of the HEO nanoparticles was ∼30 nm and homogenous element distribution was obtained from post-electrospinning thermal decomposition. The synthesized HEO NPs exhibited magnetic properties with the highest saturation magnetization at 9.588 emu g^{-1} and the highest coercivity at 147.175 Oe for HEO NPs with four magnetic elements while integrating more nonmagnetic elements will suppress the magnetic response. This electrospun and low-temperature annealing method provides an easy and flexible design for nanoparticle composition and economic processing pathway, which offers a cost- and energy-effective, and high throughput entropy nanoparticle synthesis on a large scale.

Introduction

High entropy materials with single-phase structures have drawn considerable attention owing to their unique physical and chemical properties for wide applications in biomedical,[1,2] catalysis,[3,4] and energy storage fields.[5] Recently, high entropy oxides (HEOs), high entropy chalcogenides, high entropy nitrides, and high entropy carbides have generated increased interest in the understanding and applications of this new category of advanced functional materials. High entropy oxides (HEOs) refer to the oxide system containing at least five principle elements with equimolar or near-equimolar concentration, in which the configurational entropy is larger than 1.5R in a random state, regardless of whether they are single-phase or

[a]Department of Metallurgical and Materials Engineering, The University of Alabama, Tuscaloosa 35487, AL, USA

[b]Department of Chemical and Materials Engineering, University of Nevada Reno, Reno 89557, NV, USA

[c]Department of Human Nutrition and Hospitality Management, The University of Alabama, Tuscaloosa 35487, AL, USA

[d]Materials Science Program, School for Engineering of Matter, Transport, and Energy, Arizona State University, Tempe, 85287, AZ, USA. E-mail: fengyan@asu.edu

† Electronic supplementary information (ESI) available. See DOI: https://doi.org/10.1039/d3na00090g

multiphase at room temperature.[6] The ideal configurational entropy (ΔS_{config}) for a $A_xB_yO_z$ type oxide can be given as:[7]

$$\Delta S_{\text{config}} = -R\left[x\left(\sum_{a=1}^{M} x_a \ln x_a\right)_{\text{A-site}} + y\left(\sum_{b=1}^{N} y_b \ln y_b\right)_{\text{B-site}} + z\left(\sum_{o=1}^{P} z_o \ln z_o\right)_{\text{O-site}}\right]$$

where x_a, y_b and z_o are the mole fractions of the elements in the A-site, B-site, and O^{2-}-site, respectively. M, N, and P are the number of cations present on the A-site, B-site, and O^{2-}-site, respectively.

The ΔS_{config} depends on the number of incorporated elements for high entropy materials. The stability of the system can be analyzed by the Gibbs energy according to the Gibbs–Helmholtz equation:[8]

$$\Delta G_{\text{mix}} = \Delta H_{\text{mix}} - T\Delta S_{\text{mix}}$$

It is the competition between ΔH_{mix} and $T\Delta S_{\text{mix}}$ that determines the phase selection in high entropy materials. When $T\Delta S_{\text{mix}}$ could balance or exceed ΔH_{mix}, the entropy stabilization effect appeared. More negative ΔG_{mix} indicates the increased stability of the system due to the higher configurational entropy

arising from the increasing number of elements. The entropy stabilization mechanism and flexible composition design help the formation of single-phase rocksalt, fluorite, perovskite, and spinel structures for HEOs.

HEOs exhibit good performance in several aspects, such as electrochemical catalysis,[9] electronics,[10] energy storage materials,[11] and magnetic applications.[12] The HEO system provides a large landscape for the study of magnetic properties due to their chemical complexity, which provides more bonding interaction types and crystallographic structures. The magnetic performance of oxides is related to the valence state, spin state, coordination geometry, and the bonding of metals to oxygen. A spinel-type $(Al_{1/6}Co_{1/6}Cr_{1/6}Fe_{1/6}Mn_{1/6}Ni_{1/6})_3O_4$ HEO was achieved and it possessed ferrimagnetic behavior below Curie temperature (248 K), and the long-range ferrimagnetic behavior resulted from the quite larger super-exchange interactions.[13] High entropy oxide $(Mg_{0.2}Co_{0.2}Ni_{0.2}Cu_{0.2}Zn_{0.2})O$ was reported with rocksalt structure exhibiting a sluggish magnetic transition but possesses a long-range ordered antiferromagnetic ground state. The magnetic structure consists of ferromagnetic sheets in the (111) planes of spins antiparallel between two neighboring planes.[14]

Due to the difficulties in mixing different elements with various atomic radii, oxidation states, and chemical valence as well as the chemical and physical properties, high entropy materials have great challenges to obtain specimens with a homogeneous structure. The carbothermal shock method was developed to synthesize high entropy alloy nanoparticles composed of more than five elements by a flash heating and cooling process.[15] In addition, an aerosol droplet-mediated technique was employed to synthesize the HEA nanoparticles with atomic-level mixing of immiscible metal elements.[16] Flame spray pyrolysis (FSP) route was also used to produce single-phase $(Mn, Fe, Ni, Cu, Zn)_3(O)_4$ quinary HEO NPs.[17] These HEA NPs were generated during the fast heating/quenching process, which resulted in the decomposition of the metal precursors and freezing-in of the zero-valent metal atoms simultaneously. These one-step HEO NP syntheses need rapid heating at high temperatures (~2000 K for the carbothermal shock method, ~1100 °C for the aerosol synthesis method, and ~1900 °C for the FSP method) in a short time. These methods have a high requirement for the equipment to achieve fast heating and cooling rates during the processing, which limits the yield of the high entropy nanoparticles. Applying carbon support to the synthesis of high entropy oxide is also an efficient method to generate homogeneous HEO NPs for catalytic applications.[18] However, performance degradation would happen if there is peeling off and aggregating of the nanoparticles due to the weak interfacial bonding between the nanoparticles and the carbon support.[19] Moreover, for the HEO with carbon support, the high-temperature treatment during the synthesis will result in the carbothermal reduction of the oxide.

To overcome these limitations, we propose a low-temperature two-step synthesis of HEO NPs by combining electrospinning, following air condition annealing. Electrospinning is an electrostatic fiber fabrication technique to produce fibers with diameters ranging from 2 nm to several micrometers using polymer solutions. This technique draws increased attention because of the wide applications of the nanofibers in the fields of biosensors,[20] tissue engineering,[21] drug delivery[22] as well as the energy generation aspects.[23] Electrospinning has been utilized to produce oxide nanoparticles, such as CuO nanoparticles that are electrospun from the precursor solution including copper acetate salt and polyvinyl alcohol (PVA) polymer, and then calcinated to obtain CuO nanoparticles.[24]

In this study, single-phase HEO NPs with up to eight metal elements were prepared by electrospinning and low-temperature annealing in air conditions. To mix the incorporated elements uniformly, the nitrate salt precursors were dissolved in the solution, which was applied in the electrospinning process to generate nanofibers. The cations were enveloped in the nanofibers during the electrospinning process. With low-annealing conditions in air, e.g., at 330 °C, the single-phase spinel HEO NPs could be obtained. Extremely fast heating and cooling rates are not required in this method, which lowers the synthesis requirements and provides more routes for the HEO materials. The magnetic properties of these HEO NPs were characterized. This low-temperature electrospinning-based HEO NP synthesis paves the way to fabricate upscale manufacturing of the HEO materials for functional applications.

Results and discussion

2.1 Synthesis of the HEO nanoparticles using the electrospun fibers

To prepare the precursor for the electrospinning, the starting salts of the precursors were dissolved in the CA solution (12 wt% CA solution in acetone), e.g., nitrate salts of Fe^{3+}, Co^{2+}, Ni^{2+}, Cr^{2+}, Cu^{2+}, Mg^{2+}, Zn^{2+}, and Mn^{2+} cationic elements. These salts can be fully dissolved in the CA/acetone solution by magnetic stirring overnight. As shown in Fig. 1(a), the CA/acetone solution was clear, and several types of precursors with multicomponent elements from 3 to 8 elements and labeled as 3-HEO, 4-HEO, 5-HEO, 6-HEO, 7-HEO, and 8-HEO, which are Co–Ni–Cr, Fe–Co–Ni–Cr, Fe–Co–Ni–Cr–Cu, Fe–Co–Ni–Cr–Cu–Mg, Fe–Co–Ni–Cr–Cu–Mg–Zn, and Fe–Co–Ni–Cr–Cu–Mg–Zn–Mn, respectively, were prepared. These salt CA solutions showed various colors due to the dissolved elements (see ESI Fig. S1†). The solubility of these salts can be found in ESI Table S1.† Fig. 1(a) shows the process of the electrospining of the CA fibers with these nitrate salts. The electrospun fibers are shown and majorly the fiber shown that the CA fibers and the nitrate salts were filled into the fiber after the acetone was dried. One of the fibers for HEO-8 fibers is shown in Fig. 1(a). The microstructure of the electrospun fiber was characterized using scanning electron microscopy (SEM), as shown in Fig. 1(c), where the fiber had a diameter of ~320 nm ± 17.6 nm.

As shown in Fig. 1(b), we synthesized the HEO NPs by annealing the electrospun fibers at a low temperature, such as 300 to 400 °C. The metal salt precursors were enveloped in the nanofibers during the electrospinning process. The morphology
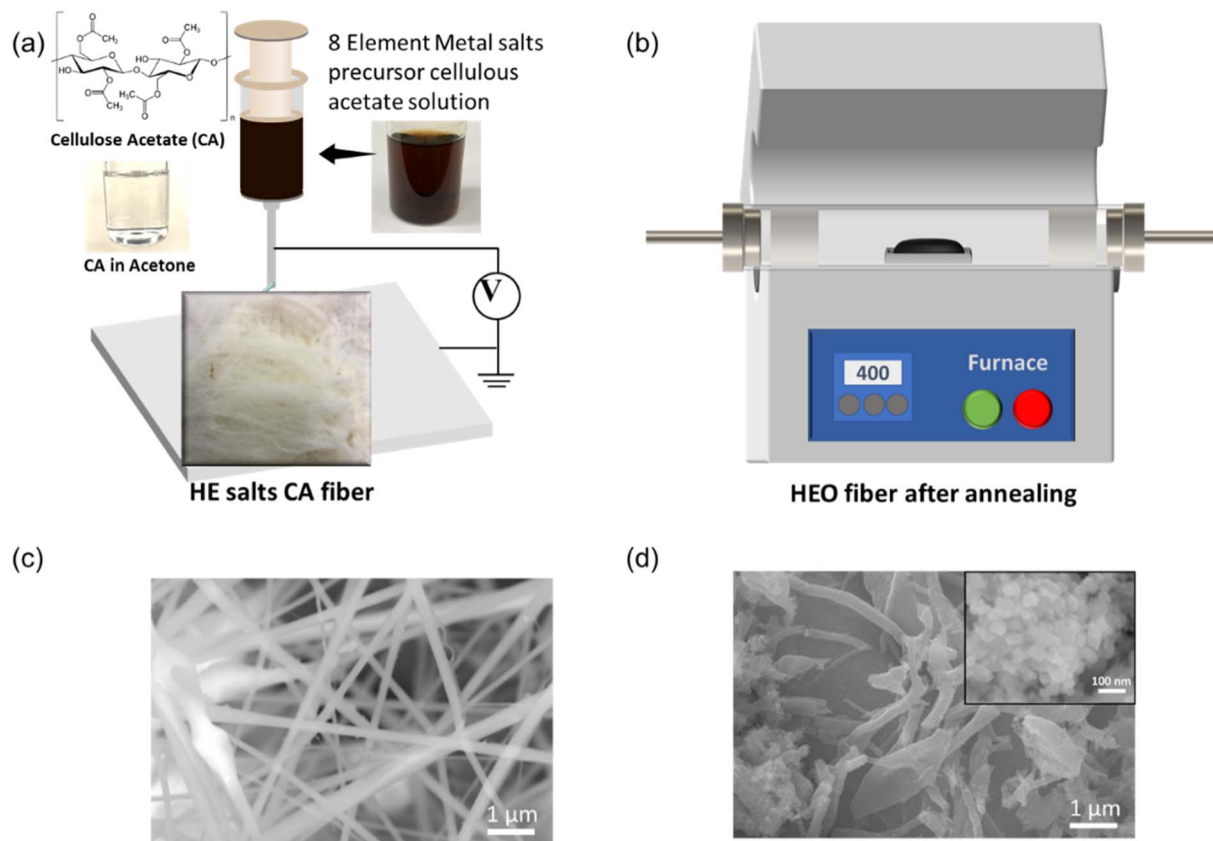
Fig. 1 The schematic of (a) the electrospun process of the metal-CA fibers with the optical images of the precursors and the electrospun fiber, and (b) electrospun fibers annealed in the air. Scanning electron microscopy morphology of the (c) as-electrospun HE-CA fibers and (d) HEO fibers after post-annealing.

of the HEO fibers was characterized using SEM, as exhibited in Fig. 1(d) for the annealed 8-HEO nanofibers. The other SEM images for 3-HEO to 7-HEO NPs are shown in ESI Fig. S1–S6.† The annealed nanofibers were distributed as broken fibers and beads shape, which is attributed to the residual strain during the forming of crystal nanoparticles while CA decomposes.[24] It can be observed that the annealed nanofibers are composited of NPs that aggregate inside the fibers.

2.2 HEO nanoparticle formation mechanisms

To explore the formation mechanism of HEO NPs, differential scanning calorimetry (DSC) was applied to determine the thermal decomposition process during the annealing of these HE-CA fibers, as shown in Fig. 2(a). The DSC of pure CA nanofibers is also included as a reference. The glass transition temperature (T_g) of CA is approximately 198 °C and the melting temperature was within the range of 230–250 °C in the reported work.[25] The endothermic peak at 310 °C reflects the decomposition of CA, respectively. Particularly, upon increasing the entropy by increasing the number of elements, the melting temperature was increased for the electrospun fibers. The first endothermic peak around 170 °C represents the dehydration of nitrate and the glass transition and the crystallization process of the CA nanofibers. The exothermic peaks at around 190 °C

exhibited the transition from hydroxide to oxides. The endothermic peak ranging from around 210–270 °C indicates that the CA decomposed in the nanofibers. Note that the CA decomposition temperature increased from 3-HEO to 5-HEO nanofibers and then reduced from 5-HEO to 8-HEO. This CA decomposition temperature was overall smaller than that of the pure CA fibers, which may contribute to the nitrate salts dehydration process release of heat to assist the CA decomposition. In addition, during the CA decomposition, which is a deacetylation process, CO_2, and CH_4 will be released from the chain scission. These released gases may provide a localized oxidization of the nitrate and lower the oxidization temperature of the HEO nanoparticles. The HEO nanoparticle formation can be described as follows: (M = Fe, Co, Ni, Cr, Cu, Mg, Zn, and Mn):

$$M(NO_3)_x \cdot aH_2O \rightarrow M(OH)(NO_3)_x \rightarrow MOOH \rightarrow MO$$

Based on the DSC results, no clear endothermic peaks beyond 300 °C were observed, thus, to fertilize the HEO NP formation, we chose the annealing temperature at 330 °C. The digital photographs of the nanofibers after the 330 °C annealing are shown in Fig. 2(b). The hypothesis about these HEO NPs detailing the formation mechanisms is shown in Fig. 2. The HE salt-CA nanofibers work as a frame for the metal nitrate salts, which disperses the metal ions and prevents their aggregation.
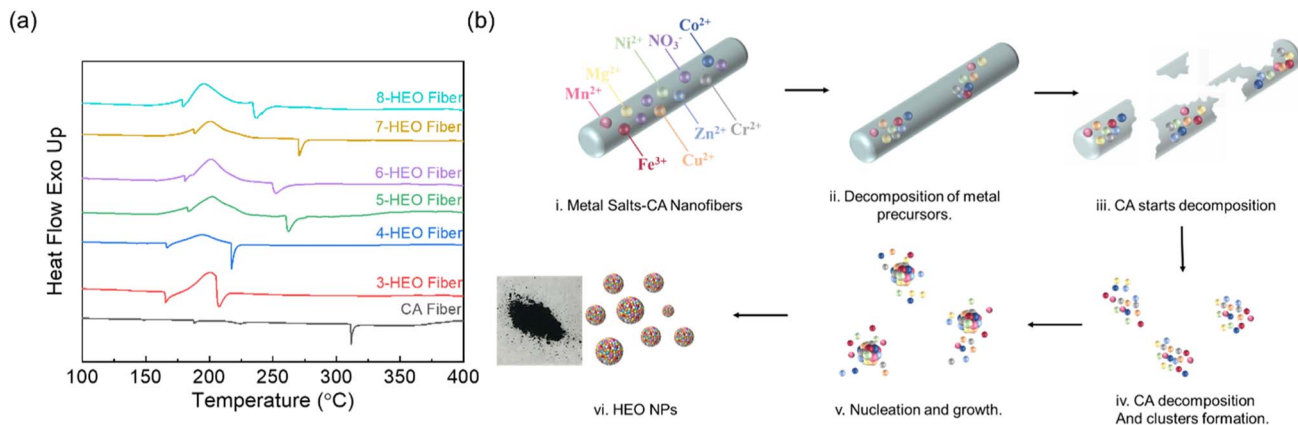
Fig. 2 (a) DSC of the fibers, and (b) proposed mechanism of HEO nanoparticles formation by converting the electrospun nanofibers *via* low-temperature annealing in air and the accomplished powder. A digital photograph of the as-synthesized HEO NPs.

With increasing annealing temperature, metal nitrate dehydration and decomposition occur. Then, the CA crystallizes and decomposes. According to the nucleation mechanism,[26,27] the HEO clusters form inside these CA nanofiber pieces and the nanofiber frames limit the further growth of nuclei by preventing the coalescence and attachment process. Finally, the nanoparticles are formed completely. This annealing temperature is much lower than that of HEO NPs synthesized using the other approach and provides a low-cost and less energy consumption approach for the HEO NPs fabrication pathway by utilizing the localized thermal release of CA decomposition and the metal nitrate dehydration and oxidization.

2.3 Microstructure and chemical states of HEO nanoparticles

The crystallinity and microstructure of the low-temperature synthesized HEO NPs were characterized using X-ray diffraction (XRD) and transition electron microscopy (TEM), respectively, as shown in Fig. 3. The XRD patterns of the HEO nanoparticles, including from three metal elements to eight
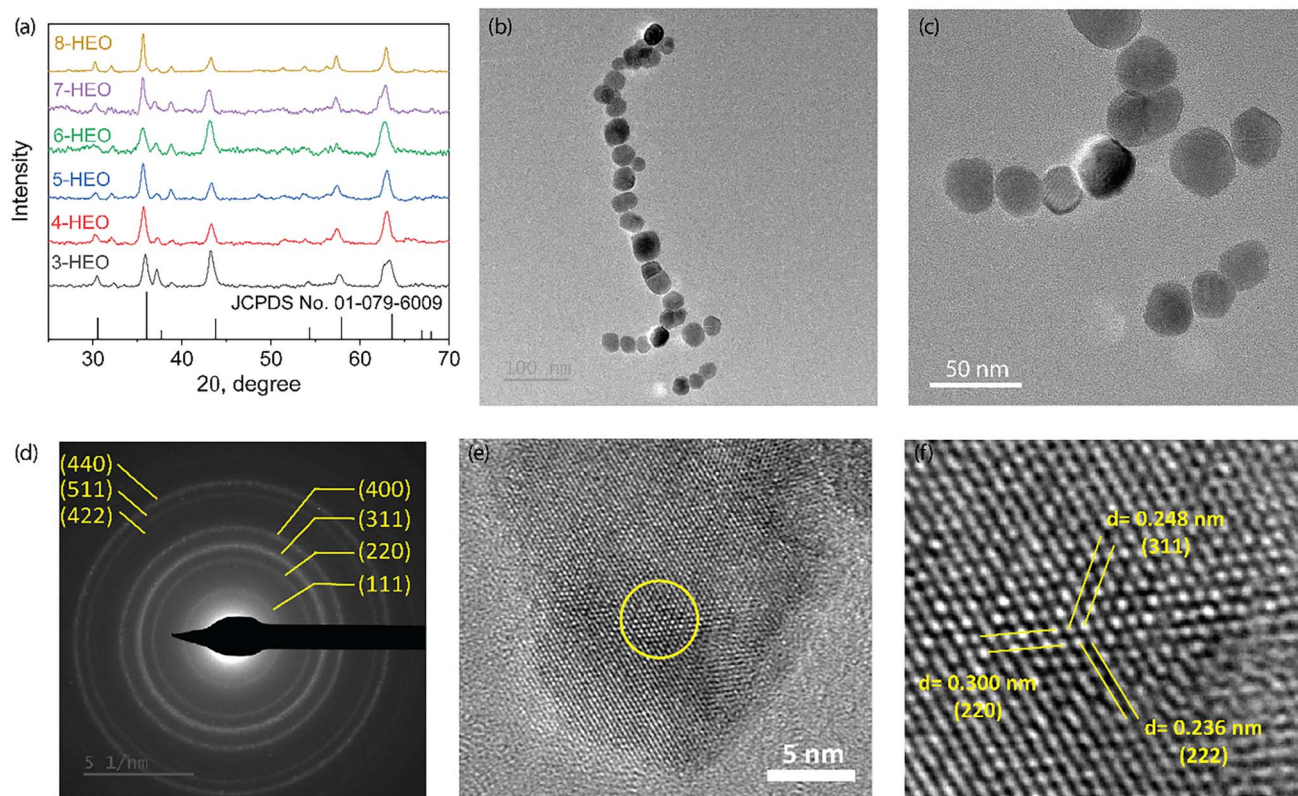

Fig. 3 (a) XRD patterns of HEO NPs with 3 elements to 8 elements. (b). STEM images of 8-HEO NPs. (c) SAED analysis of 8-HEO NPs to confirm the spinel crystal structure. (d–f) HRTEM of 8-HEO NPs.

metal elements, are shown in Fig. 3(a). The indexed XRD patterns confirmed the formation of the pure spinel cubic crystal structure for all these HEO NPs. Upon increasing the number of elements, the 2θ peak shifts slightly to the small angle, indicating that the lattice parameter may be smaller due to the different ion radii of the cations. In addition, the spinel cubic structure may also be distorted with increasing metal ions due to the peak broadening. The particle size was determined from low-magnification TEM images, as shown in Fig. 3(b) and (c); the diameter of the synthesized 8-HEO NPs was 33.7 nm $\pm$ 3.03 nm. An indexed selected area electron diffraction (SAED) was utilized to further confirm the spinel structure as shown in Fig. 3(d). The major diffraction rings with the Miller indexes of (220), (311), (222), (400), (422), (511), and (440) lattice planes correspond to the spinel crystal structure. The high-resolution TEM (HRTEM) images of 8-HEO NPs are exhibited in Fig. 3(e) and (f), which show the appearance of crystalline fringes.

High-resolution STEM images of 8-HEO nanoparticles are shown in Fig. 4(a), and the high-resolution STEM-EDX shows that these HEO NPs have 8 elements, demonstrating that our electrospun HEO nanoparticles were successfully synthesized at low temperatures. Fig. 4 also shows that the atomic percentages

of 8-HEO for each element were Fe (9.6 at%), Co (8.8 at%), Ni (8.8 at%), Cr (9.5 at%), Cu (7.3 at%), Mg (6.6 at%), Zn (6.5 at%), and Mn (9.3 at%).

To further confirm the chemical oxide state of the elements in 8-HEO, qualitative X-ray photoelectron spectroscopy (XPS) was employed, as shown in Fig. 5 and it confirmed that the metal elements were in oxidized states. Fig. 5(a) shows the XPS spectra of Fe $2p_{1/2}$ and $2p_{3/2}$ at 722.94 and 709.83 eV corresponding to the Fe^{3+}.[28] The satellite peak of Fe $2p_{3/2}$ is located at 716.60 eV. The deconvoluted Fe $2p_{1/2}$, $2p_{3/2}$, and satellite peaks confirmed the presence of Fe^{2+} and Fe^{3+} oxidation states arising from the Fe_3O_4 phase, which includes FeO and Fe_2O_3 states. The Fe^{2+} and Fe^{3+} occupy both the tetrahedral and octahedral crystal sites in spinel oxide structure.[29] From the XPS spectra, we calculated that the ratio between $Fe^{3+}/Fe^{2+} = 2:1$. The XPS spectrum of the Co 2p energy state is shown in Fig. 5(b). The Co $2p_{1/2}$ appears at 794.93 eV and Co $2p_{3/2}$ appears at 779.36 eV due to the split spinning orbital, where the splitting energy difference is 15.57 eV. The satellite peak of Co is located at 785.56 eV. The spectrum of Co indicates the co-existence of Co^{2+} and Co^{3+} oxidation states and the ratio $Co^{2+}/Co^{3+} = 1:2$.[30] In the Ni XPS spectrum, as shown in Fig. 5(c), Ni $2p_{1/2}$ and Ni $2p_{3/2}$ can be
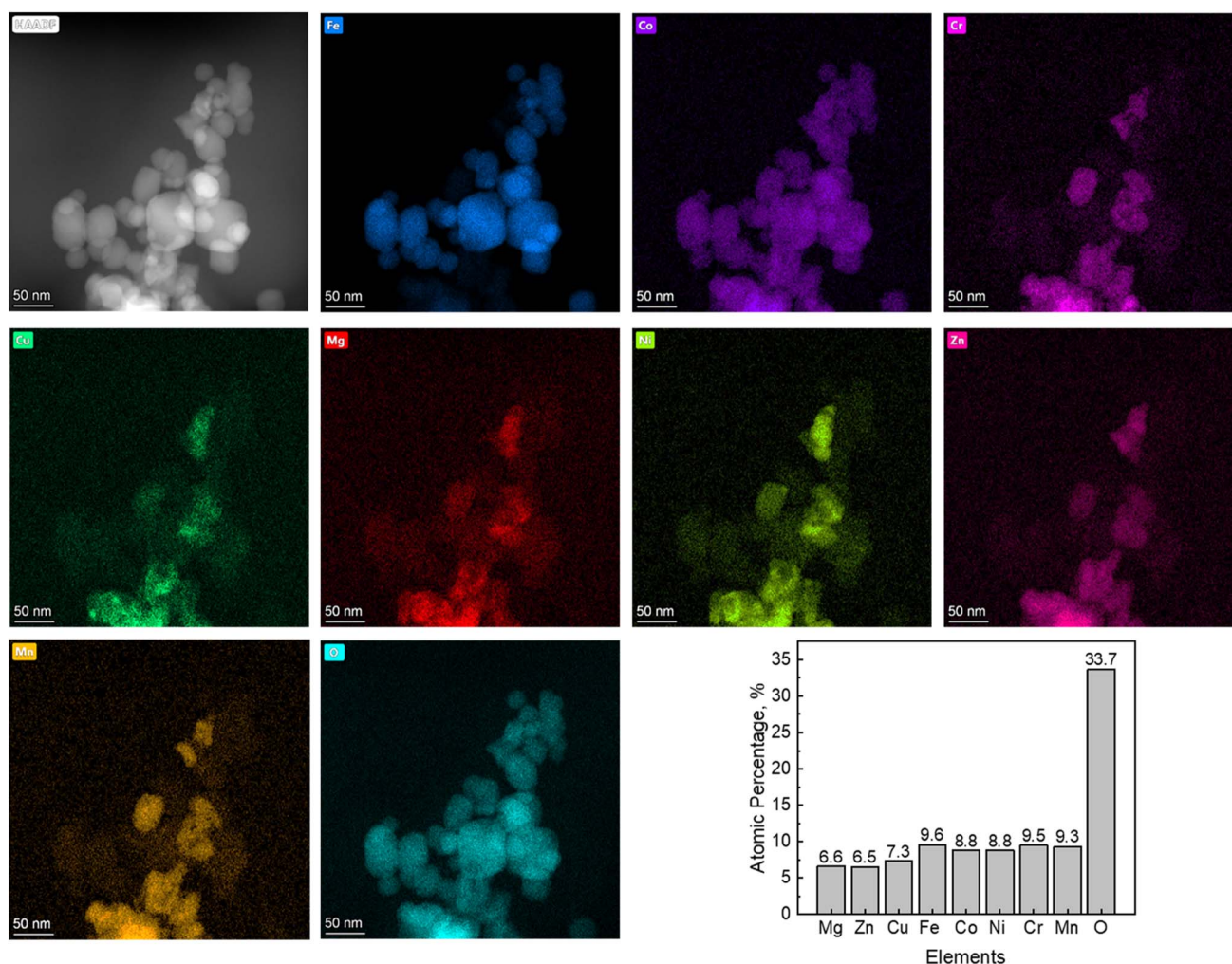

Fig. 4 STEM and EDS mapping of 8-HEO NPsEDS elemental mapping of all eight individual metal elements and oxygen.
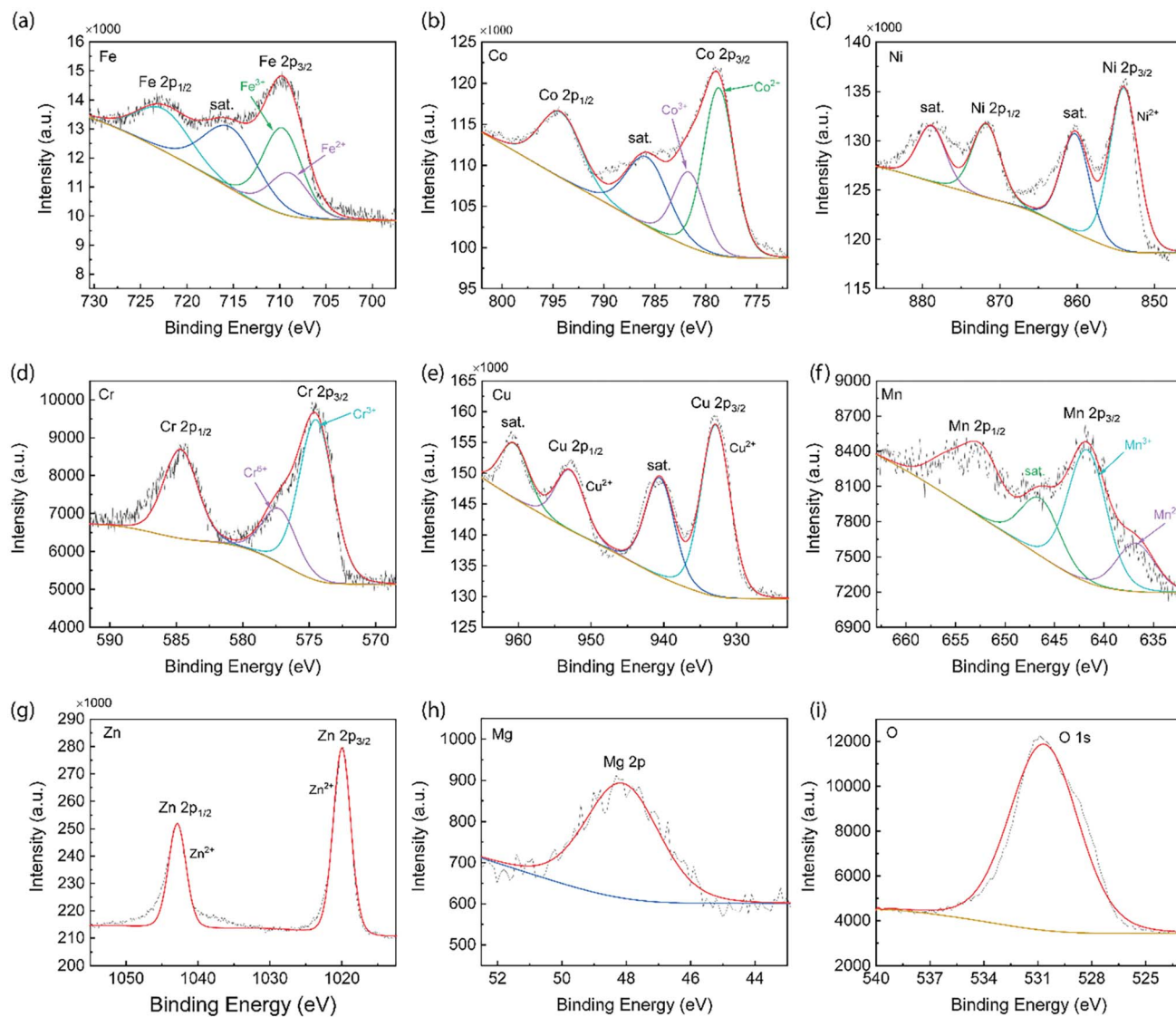
Fig. 5   XPS analysis of 8-HEO NPs. (a) Fe 2p, (b) Co 2p, (c) Ni 2p, (d) Cr 2p, (e) Cu 2p, (f) Mn 2p, (g) Zn 2p, (h) Mg 2p, and (i) O 1s.
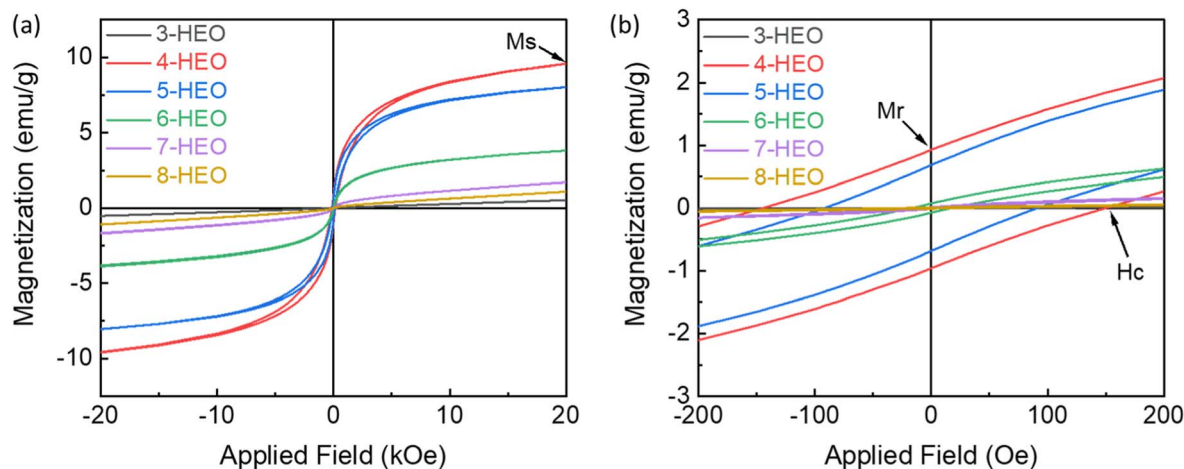

Fig. 6   (a) Room temperature magnetic hysteresis loop of 3 to 8-HEO NPs and (b) the magnetization curves at low magnetic field region (yellow box region).

Table 1 Magnetic properties of series of HEO samples

Samples	Metal elements	H_c (Oe)	M_s (emu g^{-1})	M_r (emu g^{-1})
3-HEO	CoNiCr	50.090	0.525	2.203×10^{-3}
4-HEO	FeCoNiCr	147.175	9.588	0.944
5-HEO	FeCoNiCrCu	91.505	8.035	0.685
6-HEO	FeCoNiCrCuMg	17.016	3.849	74.160×10^{-3}
7-HEO	FeCoNiCrCuMgZn	9.586	1.706	14.210×10^{-3}
8-HEO	FeCoNiCrCuMgZnMn	29.047	1.090	10.102×10^{-3}

observed at 871.78 and 854.02 eV. Two satellite peaks at 879.00 eV (Ni 2p$_{1/2}$) and 860.29 (Ni 2p$_{3/2}$) eV were observed. The Ni 2p$_{3/2}$ peak confirms the presence of a Ni^{2+} oxidation state.[31] The Cr XPS spectrum is shown in Fig. 5(d) and the peaks at the binding energy of 585.04 and 575.16 eV represent Cr 2p$_{1/2}$ and Cr 2p$_{3/2}$ signals, which indicate the presence of Cr^{3+} and balanced by Cr^{6+} and the ratio of Cr^{3+}/Cr^{6+} is 3 : 1.[3,32] The Cu XPS spectrum shown in Fig. 5(e) exhibits the Cu 2p$_{1/2}$ and Cu 2p$_{3/2}$ peaks at 953.16 and 932.95 eV, respectively. The satellite peaks are located at 961.10 and 940.725 eV, corresponding to Cu 2p$_{1/2}$ and Cu 2p$_{3/2}$, respectively. The split Cu 2p$_{1/2}$, Cu 2p$_{3/2}$, and satellite peaks prove that Cu is in a 2+ oxidation state.[33] Fig. 5(f) shows the XPS spectrum of the Mn element and the Mn 2p$_{1/2}$ and Mn 2p$_{3/2}$ peaks were located at 653.50 and 641.84 eV, respectively. Mn 2p$_{3/2}$ comprises two components with binding energies of 642.85 and 636.84 eV, which are attributed to Mn^{3+} and Mn^{2+} oxidation states. The co-existence of Mn^{3+} and Mn^{2+} oxidation states indicates that the Mn in HEO NPs spinel structure occupies the tetrahedral and octahedral crystal sites with Mn^{3+}/Mn^{2+} = 3 : 1.[34,35] The Zn XPS spectrum is exhibited in Fig. 5(g) and the two split peaks are located at 1042.86 and 1020.05 eV, which are assigned to Zn 2p$_{1/2}$ and Zn 2p$_{3/2}$ of tetrahedral Zn^{2+}, confirming that Zn is in 2+ oxidation state in the spinel HEO NPs.[36] The Mg XPS spectrum generally uses Mg 1s to analyze the oxidation state, which is located between 1302 and 1305 eV.[37] However, the binding energy of Mg 1s is out of the scan range of the equipment we used in this study. Therefore, Mg 2p was used for the Mg oxidation state analysis. The XPS spectrum of Mg 2p is located at 48.14 eV, as is shown in Fig. 5(h), which confirmed the 2+ oxidation state of Mg in the HEO NPs structure.[38] The XPS spectrum of O shows the O 1s at 530.76 eV, which represents the lattice oxygen of metal–oxygen bonds for the spinel HEO NPs.[39] The multivalence for these metal cations will contribute to the spin fluctuations in HEO NPs and should contribute to the improved magnetic properties.

2.4 Magnetic response of HEO nanoparticles

Since the direct magnetic interactions between the metals in the HEOs are limited, the indirect exchange interactions between the metal cations and oxygen anions and cations are more common.[40] The magnetic property of HEO NPs, including those with 3 metal elements to 8 metal elements, was measured up to 20 kOe magnetic field at room temperature as shown in Fig. 6. These magnetic hysteresis loops indicated the presence of magnetic moments in the HEO NPs and the magnetic moments

aligned under the applied magnetic field. The magnetic parameters such as coercivity (H_c), saturation magnetization (M_s), and remanence magnetization (M_r) are summarized in Table 1. It was shown that the transition metal HEOs, such as 3-HEO, 4-HEO, and 5 HEO with Fe, Co, Ni, Cr, and Mn show high H_c, while the HEOs with nonmagnetic elements, such as Cu, Mg, and Zn will weaken the magnetic properties. For example, the 4-HEO NPs possess the highest M_s with 9.588 emu g^{-1} and M_s decreases with the addition of Cu and Cu/Mg and Cu/Mg/Zn for 5-HEO, 6-HEO, and 7-HEO, respectively. The remanence magnetization follows a similar trend of saturation magnetization, as shown in Table 1.

It was reported that Cu ions will decrease in the spin ordering parameter in the oxides, where the Cu concentration will impact the degree of spin frustration in the magnetic lattice.[41] The addition of nonmagnetic Zn^{2+} ion into the system would also decrease the M_s resulting from the replacement of magnetic Co^{2+} and Ni^{2+} ions by Zn^{2+} due to the lower magnetocrystalline anisotropy of Zn than that of Ni and Co.[42] Increasing the magnetic Mn concentration can increase the saturation magnetization in Zn$_{0.3}$Mn$_x$Fe$_{2.7-x}$O$_4$ NPs due to the distribution of Mn^{2+} ions in tetrahedral and octahedral sites.[43] Thus, it is believed that by tailoring the magnetic metals in HEOs, higher magnetic properties can be further developed by preventing non-magnetic elements. As for the fundamental results of the variation of the magnetic properties, we will investigate them in future work.

Conclusions

In summary, we demonstrate a low-cost, low-temperature, and scalable synthesis approach of single-phase spinel magnetic HEO NPs including up to eight metal elements by utilizing electrospun and post-electrospun ambient annealing processes. The metal nitrate precursors were enveloped in cellulose acetate nanofibers during electrospinning. The homogenous HEO NPs could be generated by annealing the nanofibers at 330 °C for 30 minutes. The 8-HEO (Fe–Co–Ni–Cr–Cu–Mg–Zn–Mn) NPs possess a diameter of 33.7 nm and the spinel single-phase structure was confirmed with the uniform elemental distribution. The XPS spectrum of each element proves the oxidation state of HEO NPs and demonstrates the multivalent of the magnetic elements in the spinel structure. This electrospinning method possesses several advantages including the low-temperature synthesis of HEOs, uniform premixture in the precursors of the metal ions, flexibility to tune the elements in

HEOs, and low cost of the HEO nanoparticles for upscale manufacturing. With this newly developed method, we can obtain pure HEO NPs by leveraging biomass materials to reduce the thermal budget and provide large-scale manufacturing capability to synthesize HEO nanomaterials or even other high entropy materials.

Experiment methods

High entropy oxide nanoparticles fabrication

The metal nitrate precursor salts used were $Fe(NO_3)_3$ $9H_2O$ (Acros Organics, 99%), $Co(NO_3)_2$ $6H_2O$ (Acros Organics, 99%), $Ni(NO_3)_2$ $6H_2O$ (Alfa Aesar, 99.99%), $Cr(NO_3)_3$ $9H_2O$ (Strem Chemicals, 99%), $Cu(NO_3)_2$ $3H_2O$ (Acros Organics, 99%), $Mg(NO_3)_2$ $6H_2O$ (Acros Organics, 99%), $Zn(NO_3)_2 \cdot 6H_2O$ (Alfa Aesar, 99%) and $Mn(NO_3)_2$ xH_2O (Thermo Fisher, 99.99%). The cellulose acetate (CA, Acros Organics) 12% (w/v) solution with acetone as a solvent. The precursor solution (1.0 mol L^{-1}) was prepared by dissolving various nitrate salts (having equimolar concentration) in the CA solution. After completely dissolved solution formation, the spinning precursor solution was loaded into a 10 mL syringe (Becton, Dickinson and Company, Franklin Lakes, NJ, USA) with a 22-gauge blunt needle (Hamilton Company, Reno, NV, USA) as the spinneret. The nickel nitrate-loaded fibers were then spun. After the spinning process, the nanofibers formed on the aluminum foil directly beneath the spinneret tip were collected and annealed at 330 °C for 30 min in a box oven with an adequate supply of oxygen flow.

High entropy oxide nanoparticle characterizations

The HEO NPs were analyzed by X-ray diffraction (XRD), Philips X'Pert MPD X-ray diffractometer with Cu Kα ($\lambda = 1.5405$ Å), and scanning electron microscopy (SEM, JEOL 7000 FE). The chemical composition of HEO NPs was characterized by energy-dispersive X-ray spectroscopy (EDS) attached to the SEM. Thermal stability and phase transformation behaviors of the HEO NPs were evaluated using TA DSC 2500 at a heating/cooling rate of 20 K min^{-1} with N_2 gas. X-ray photoelectron spectroscopy (XPS) was recorded using the Kratos Axis XPS system equipped with a monochromated Al X-ray source. The particle structure and sizes of the HEO NPs were examined with a Scanning Transmission Electron Microscope (STEM), FEI Talos F200s, which was operated at 200 kV, and equipped with a high angle annular dark field (HAADF) detector and EDX energy dispersive X-ray system. All of the investigated powder samples were sonicated in ethanol for 10 min and then deposited onto an ultrathin carbon-coated Cu grid (from Ted Pella) using a glass pipette. A vibrating sample magnetometer (VSM) was used to characterize the magnetic properties of the HEO NPs powder by applying a magnetic field up to 2T.

Data availability

Research data are available based on reasonable request to the corresponding author.

Author contributions

L. L and F. Y had the idea, design the experiments, and led the investigation. X. H synthesized the HEO NPs. D. L, Y. Z. carried out the STEM characterization, S. N. V performed the XPS characterization, J. Z., and L. K conducted the DSC characterization.

Conflicts of interest

The authors declare no competing financial interests.

References

1 W. Wang, K. Yang, Q. Wang, P. Dai, H. Fang, F. Wu, Q. Guo, P. K. Liaw and N. Hua, *J. Alloys Compd.*, 2022, 164383.

2 S. Schönecker, X. Li, D. Wei, S. Nozaki, H. Kato, L. Vitos and X. Li, *Mater. Des.*, 2022, **215**, 110430.

3 D. Wang, S. Jiang, C. Duan, J. Mao, Y. Dong, K. Dong, Z. Wang, S. Luo, Y. Liu and X. Qi, *J. Alloys Compd.*, 2020, **844**, 156158.

4 C. Zhan, Y. Xu, L. Bu, H. Zhu, Y. Feng, T. Yang, Y. Zhang, Z. Yang, B. Huang and Q. Shao, *Nat. Commun.*, 2021, **12**, 1–8.

5 H. Shen, J. Zhang, J. Hu, J. Zhang, Y. Mao, H. Xiao, X. Zhou and X. Zu, *Nanomaterials*, 2019, **9**, 248.

6 A. Sarkar, Q. Wang, A. Schiele, M. R. Chellali, S. S. Bhattacharya, D. Wang, T. Brezesinski, H. Hahn, L. Velasco and B. Breitung, *Adv. Mater.*, 2019, **31**, 1806236.

7 A. Sarkar, B. Breitung and H. Hahn, *Scr. Mater.*, 2020, **187**, 43–48.

8 M. C. Gao, J.-W. Yeh, P. K. Liaw and Y. Zhang, *High-Entropy Alloys (HEA): Fundamentals and Applications*, Springer International Publishing, Cham, United States, 2016.

9 S. H. Albedwawi, A. AlJaberi, G. N. Haidemenopoulos and K. Polychronopoulou, *Mater. Des.*, 2021, **202**, 109534.

10 A. Mikuła, J. Dąbrowa, A. Kusior, K. Mars, R. Lach and M. Kubowicz, *Dalton Trans.*, 2021, **50**, 9560–9573.

11 A. Sarkar, L. Velasco, D. Wang, Q. Wang, G. Talasila, L. de Biasi, C. Kübel, T. Brezesinski, S. S. Bhattacharya and H. Hahn, *Nat. Commun.*, 2018, **9**, 1–9.

12 R. Witte, A. Sarkar, L. Velasco, R. Kruk, R. A. Brand, B. Eggert, K. Ollefs, E. Weschke, H. Wende and H. Hahn, *J. Appl. Phys.*, 2020, **127**, 185109.

13 A. Mao, H.-X. Xie, H.-Z. Xiang, Z.-G. Zhang, H. Zhang and S. Ran, *J. Magn. Magn. Mater.*, 2020, **503**, 166594.

14 J. Zhang, J. Yan, S. Calder, Q. Zheng, M. A. McGuire, D. L. Abernathy, Y. Ren, S. H. Lapidus, K. Page and H. Zheng, *Chem. Mater.*, 2019, **31**, 3705–3711.

15 Y. Yao, Z. Huang, P. Xie, S. D. Lacey, R. J. Jacob, H. Xie, F. Chen, A. Nie, T. Pu and M. Rehwoldt, *Science*, 2018, **359**, 1489–1494.

16 Y. Yang, B. Song, X. Ke, F. Xu, K. N. Bozhilov, L. Hu, R. Shahbazian-Yassar and M. R. Zachariah, *Langmuir*, 2020, **36**, 1985–1992.

17 A. H. Phakatkar, M. T. Saray, M. G. Rasul, L. V. Sorokina, T. G. Ritter, T. Shokuhfar and R. Shahbazian-Yassar, *Langmuir*, 2021, **37**, 9059–9068.

18 T. Li, Y. Yao, B. H. Ko, Z. Huang, Q. Dong, J. Gao, W. Chen, J. Li, S. Li and X. Wang, *Adv. Funct. Mater.*, 2021, **31**, 2010561.

19 Y. Liang, H. Wang, P. Diao, W. Chang, G. Hong, Y. Li, M. Gong, L. Xie, J. Zhou and J. Wang, *J. Am. Chem. Soc.*, 2012, **134**, 15849–15857.

20 M. Zhang, X. Zhao, G. Zhang, G. Wei and Z. Su, *J. Mater. Chem. B*, 2017, **5**, 1699–1711.

21 K. Ghosal, C. Agatemor, Z. Špitálsky, S. Thomas and E. Kny, *Chem. Eng. J.*, 2019, **358**, 1262–1278.

22 X. Hu, S. Liu, G. Zhou, Y. Huang, Z. Xie and X. Jing, *J. Controlled Release*, 2014, **185**, 12–21.

23 S. Cavaliere, S. Subianto, I. Savych, D. J. Jones and J. Rozière, *Energy Environ. Sci.*, 2011, **4**, 4761–4785.

24 A. Khalil, M. Jouiad, M. Khraisheh and R. Hashaikeh, *J. Nanomater.*, 2014, **2014**, 1–7.

25 R. Erdmann, S. Kabasci and H.-P. Heim, *Polymers*, 2021, **13**, 1356.

26 A. S. Myerson and B. L. Trout, *Science*, 2013, **341**, 855–856.

27 K.-J. Wu, C. Edmund, C. Shang and Z. Guo, *Prog. Mater. Sci.*, 2022, **123**, 100821.

28 D. Wilson and M. Langell, *Appl. Surf. Sci.*, 2014, **303**, 6–13.

29 T. Yamashita and P. Hayes, *Appl. Surf. Sci.*, 2008, **254**, 2441–2449.

30 T. X. Nguyen, J. Patra, J.-K. Chang and J.-M. Ting, *J. Mater. Chem. A*, 2020, **8**, 18963–18973.

31 D. Wang, Z. Liu, S. Du, Y. Zhang, H. Li, Z. Xiao, W. Chen, R. Chen, Y. Wang and Y. Zou, *J. Mater. Chem. A*, 2019, **7**, 24211–24216.

32 Y. Zheng, X. Wu, X. Lan and R. Hu, *Processes*, 2021, **10**, 49.

33 Z. Li, H. Chen and W. Liu, *Catalysts*, 2018, **8**, 557.

34 A. Ramírez, P. Hillebrand, D. Stellmach, M. M. May, P. Bogdanoff and S. Fiechter, *J. Phys. Chem. C*, 2014, **118**, 14073–14081.

35 R. Tholkappiyan, A. N. Naveen, K. Vishista and F. Hamed, *J. Taibah Univ. Sci.*, 2018, **12**, 669–677.

36 R. Al-Gaashani, S. Radiman, A. Daud, N. Tabet and Y. Al-Douri, *Ceram. Int.*, 2013, **39**, 2283–2292.

37 M. V. Morales, J. M. Conesa, I. Rodríguez-Ramos, M. Rocha, C. Freire and A. Guerrero-Ruiz, *Int. J. Green Technol.*, 2017, **3**, 51–62.

38 F. Khairallah and A. Glisenti, *Surf. Sci. Spectra*, 2006, **13**, 58–71.

39 Z. Lei, X. Liu, R. Li, H. Wang, Y. Wu and Z. Lu, *Scr. Mater.*, 2018, **146**, 340–343.

40 N. Dragoe and D. Bérardan, *Science*, 2019, **366**, 573–574.

41 P. B. Meisenheimer, L. D. Williams, S. H. Sung, J. Gim, P. Shafer, G. N. Kotsonis, J.-P. Maria, M. Trassin, R. Hovden and E. Kioupakis, *Phys. Rev. Mater.*, 2019, **3**, 104420.

42 A. Mao, H.-Z. Xiang, Z.-G. Zhang, K. Kuramoto, H. Zhang and Y. Jia, *J. Magn. Magn. Mater.*, 2020, **497**, 165884.

43 B. Rezaei, A. Kermanpur and S. Labbaf, *J. Magn. Magn. Mater.*, 2019, **481**, 16–24.